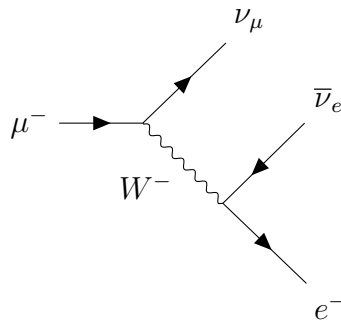




School of Physics and Astronomy

Senior Honours Project

Exploring the variations in Muon Detection with Solar Flares,
Metal Shielding, and Atmospheric Pressure



Patrick F.P. Norton
November 2023

Abstract

This project aims to investigate the correlation between the detection of cosmic ray muons and various factors, including the influence of solar flares, metal shielding and variations in atmospheric pressure. Employing various experimental methodologies and analytical techniques, 46% of X-Class solar flares were assigned to Forbush Decreases ranging from a 6% to 14% drop in muon counts. A negative correlation between atmospheric pressure and muon counts was identified and matched with literature expectations. The muon momentum spectrum of orders of $10^{-1} GeV/c$ were reconstructed and ultimately the positive muon half-life $\tau^+ = 2.174 \pm 0.015 \mu s$ was calculated to a 1% systematic error from literature value.

Declaration

I declare that this project and report is my own work.

Signature: Patrick F.P. Norton

Date: 31/11/2023

Supervisor: Dr. M. D. Needham

10 Weeks

Contents

1	Introduction	2
2	Background	2
2.1	Muon Physics	2
2.2	External Factors That Can Affect Muon Counts	5
3	Methods	7
3.1	Detector Specifications & Calibration	7
3.2	Raw Data Processing	8
4	Experiment 1 - Muon Counts After Solar Flares	9
4.1	Experimental Setup	9
4.2	Results & Analysis	9
5	Experiment 2 - Muon Momentum Spectra	11
5.1	Experimental Setup	11
5.2	Results & Analysis	11
6	Experiment 3 - Muon Count Vs. Pressure	13
6.1	Experimental Setup	13
6.2	Results & Analysis	13
7	Experiment 4 - Muon Decay Half-life	15
7.1	Experimental Setup	15
7.2	Results & Analysis	15
7.2.1	Fermi Coupling Constant	16
8	Conclusion	17
9	Acknowledgements	18
10	References	19
A	Appendix: Derivation of τ^+	21
B	Appendix: Complete Solar Flare Data 2013	22

1 Introduction

The study begins by introducing the theoretical aspects of muons, covering their origin, decay characteristics, charge ratio, and connection to the Fermi coupling constant. The report then explores the theory of external factors influencing muon counts, such as Forbush Decreases and stopping ranges followed by a detailed examination of the procedures used for data collection.

Expanding on the theoretical groundwork, the research experimentally explores the correlation between the detection of cosmic ray muons and diverse external variables, such as solar flares, the use of steel plate shielding, and atmospheric pressure fluctuations. Notably, the investigation concludes in experimentally determining the positive muons half-life and Fermi Coupling Constant, thereby advancing our comprehension of muon behaviour. In summary, the study aims to deepen our insight into fundamental particles and astrophysical phenomena by uncovering the intricate connections between cosmic ray muon detection and external influences. Specifically, this work holds importance in advancing technologies for particle detection processing and interpreting the effects of a range of solar and meteorological occurrences.

2 Background

2.1 Muon Physics

The Muon

Throughout this investigation, the focus will centre on the exploration and analysis of the muon (μ). However, before embarking on this, grasping an understanding of what the muon is is crucial. The muon is an elementary particle within the standard model that exhibits analogous traits to the electron, such as spin and electric charge. Notably, the muon distinguishes itself from the electron due to two key features. Firstly, it possesses a considerably greater mass ($M_\mu = 105.7\text{MeV}/c^2$), which is approximately 207 times larger than that of the electron [2?]. And secondly, the muon is defined by its inherent instability, decaying with an average lifetime of $\tau_\mu = 2.196\mu\text{s}$ [3]. We will revisit the details of the muon decay shortly. But first, to further understand the behaviour of muons, it is important to specify the sources of our muons.

Our Muon Source

The primary source of muons for this experiment comes from cosmic rays. Cosmic rays are energetically charged particles consisting mainly of 98% protons and other heavy nuclei, and 2% electrons [4]. Originating from astrophysical sources like the sun and intense processes within galaxies, these cosmic rays traverse space at nearly the speed of light. These rays cover a wide energy range, ranging from 1 GeV (comparable to a modest particle accelerator) to an impressive 10^8 TeV, exceeding the beam energy of the LHC collider by a significant margin [5].

A constant flux of these high-energy rays reach the upper atmosphere of the earth and upon colliding with air molecules generate a cascade of secondary particles, including protons, neutrons, pions, kaons, photons, and electrons [4]. While most of these particles are deflected back into space by the magnetosphere or heliosphere, a smaller fraction can penetrate and reach the Earth's surface [5]. The resulting particles undergo additional nuclear and electromagnetic interactions, leading to the generation of a cascade of secondary particles [6], as illustrated in Figure 1.

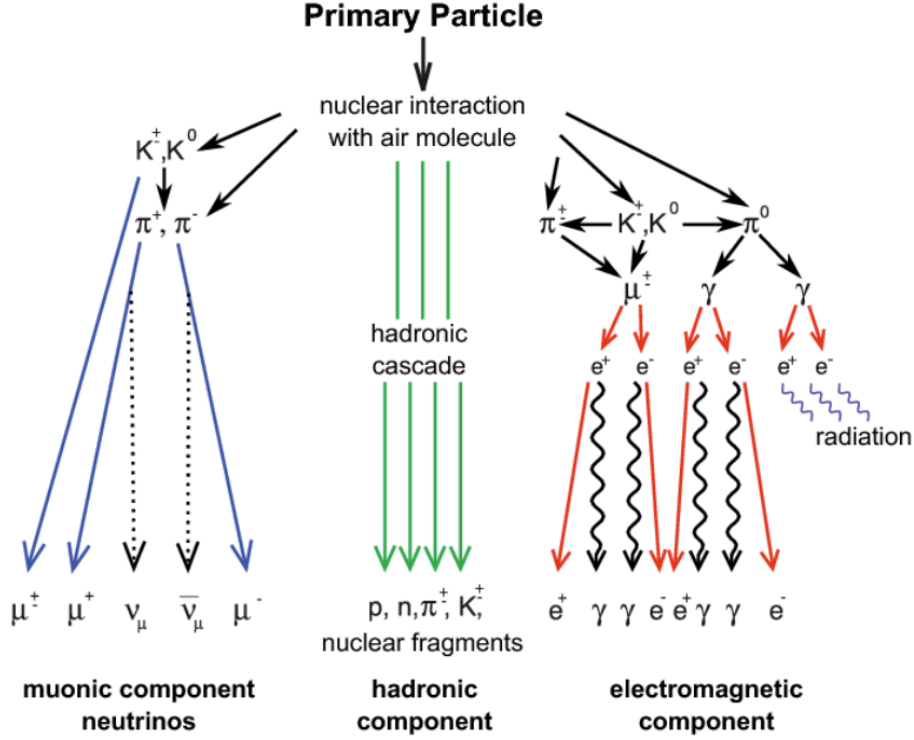


Figure 1: Cosmic ray primary particle collides with air molecule in the atmosphere [5].

Of particular interest is the process associated with the muonic component created in the shower. Pions either decay via the strong force with air nuclei, while others undergo spontaneous decay through the weak force [5]. The resulting production is of a mixture of both positively charged (μ^+) and negatively charged (μ^-) muons, neutrinos and antineutrinos as shown in the equations below:

$$\pi^+ \rightarrow \mu^+ + \nu_\mu \quad (1)$$

$$\pi^- \rightarrow \mu^- + \bar{\nu}_\mu \quad (2)$$

Muon Decay

The muon, distinct in its interaction properties, travels a relatively long distance, gradually losing kinetic energy [6]. Eventually, it can decay itself via the weak force into an electron, along with a neutrino and antineutrino as shown below:

$$\mu^- \rightarrow e^- + \nu_\mu + \bar{\nu}_e \quad (3)$$

$$\mu^+ \rightarrow e^+ + \bar{\nu}_\mu + \nu_e \quad (4)$$

The average lifetime of this mechanism, known as the “free space value,” is accurately measured to be $\tau_\mu = 2.1969811 \pm 0.0000022 \mu\text{s}$ by the Particle Data Group [3].

Muon Charge Ratio

As mentioned, the muon flux resulting from air showers comprises a mixture of both positively charged μ^+ and negatively charged μ^- muons. When evaluating the lifetime of naturally occurring muons, the observed lifetime τ_{obs} reflects a combination of positive and negative muon decay [4]. However, it will be seen that the half-life of negative muons is less than the half-life of positively charged muons at sea level [7].

The reason behind this difference in lifetime lies in the ability of **negative muons** to bind to carbon and hydrogen nuclei, circumventing the Pauli exclusion principle. This introduces an additional decay interaction with protons, $\mu^- + p \rightarrow n + \nu_\mu$, impacting the effective lifetime of μ^- [7].

For a stationary negative muon, the likelihood of nuclear absorption by a nucleus is proportionate to Z^4 , where Z represents the atomic number. Confined in an atomic orbital, with a reduced Bohr radius, resulting from a larger mass, increases the likelihood of being absorbed by the nucleus. The probability density within the nucleus scales with Z^3 , and once inside, the encounter with a proton scales like Z , resulting in an absorption probability proportional to Z^4 . This heightened absorption probability phenomenon is **exclusive to negatively charged muons**, contributing to the observed discrepancy in lifetimes [4, 7].

Hence, to attain a lifetime in line with the true “free space value” or in other words, the vacuum lifetime, calculating the half-life of the positive muon μ^+ is needed. The reason being that the positive muon lifetime closely resembles this “free space value” given that it mostly exhibits the decay mode of equation (4) analogous to being in a vacuum. To do so will require distinguishing between positive and negative muon lifetimes. For this, we derive an equation for finding τ^+ in Appendix A [4]. The result of which gives:

$$\tau^+ = \frac{\rho \tau^- \tau_{\text{obs}}}{\tau^- (\rho + 1) - \tau_{\text{obs}}} \quad (5)$$

Here, τ^+ denotes the half-life of positive muons, τ_{obs} is the observed half-life and τ^- is the half-life of negative muons. The surface flux ratio, denoted as ρ , represents the ratio of positive to negative muons and has been precisely measured as $\rho = 1.2766 \pm 0.0032$ by the CMS experiment at CERN [7].

This equation plays a crucial role in extracting the half-life of positive muons τ^+ which are not altered by the aforementioned mechanisms.

Fermi Coupling Constant

The decay of the positive muons is therefore governed by the weak force, and the strength of this force is quantified by the Fermi coupling constant, G_F . A straightforward relationship exists between the muon lifetime, τ_μ , and G_F :

$$G_F = \left(\frac{192\pi^3\hbar^7}{\tau_\mu m^5 c^4} \right)^{1/2} \quad (6)$$

Here, m denotes the rest mass of the muon, while the other symbols retain their standard meanings. When employing an instrument to measure τ_μ , it can yield a corresponding value for G_F . This proves to be useful to determine how effectively the detected muon interacts via the weak force and also because it is a useful method to measure G_F itself [4, 8].

2.2 External Factors That Can Affect Muon Counts

Solar Flares

A solar flare is a sudden burst of energy, particles and radiation emanating from the Sun's surface. It is often accompanied by the release of a large number of charged particles, including protons and electrons, into space. The energy released during a solar flare can significantly impact the space environment and affect various celestial bodies, including Earth [10].

Solar flares are classified based on their strength, with X-class flares being the most powerful with a peak flux of 10^{-4}W/m^2 as measured by the GOES spacecraft [9]. The energy released during X-class flares have a significant impact on space weather and can lead to various space-related phenomena, including Forbush decreases in cosmic ray intensity on Earth [6, 11].

Forbush Decrease

The term “Forbush decrease” refers to a reduction in the intensity of cosmic rays that enter Earth's atmosphere. These decreases are typically observed following a solar flare or coronal mass ejection (CME) from the Sun [11]. A Forbush decrease normally causes at least a 10% reduction in galactic cosmic rays on Earth, but the reduction in muon counts can be seen to range from about 3% to 20% [12].

It is important to note that many solar flares, **though not all**, are often accompanied by Forbush decreases. In such instances, the cosmic-ray intensity experiences a simultaneous decline with the earth's magnetic field, reaching a minimum of a few percent below normal. Following this, as the magnetic field undergoes recovery, the cosmic-ray intensity returns to its usual value. Since Forbush decreases manifest as a global phenomenon, the mechanism responsible for them (largely unidentified to date) must influence both low-energy primary particles, reaching Earth's atmosphere primarily near the magnetic poles, and high-energy particles capable of arriving in all directions [6, 13].

Although the physics explaining the cause of the Forbush decrease is not precisely known, it is thought that the main phase of the magnetic storm may result from the injection of solar plasma into the magnetosphere region. In this region, Earth’s magnetic field predominates over the entire interplanetary field. This would cause the plasma pressure to increase, pushing the field line forces apart thus affecting the earth’s magnetosphere and overall field strength [6].

Muon Stopping Power and Ranges

The stopping rate of muons depends on their initial energy and the nature of the material they traverse. The mean muon-stopping ranges in matter can be explained by the following equation:

$$-\frac{dE}{dX_i} = a(E) + b(E)E,$$

where $b(E)$ represents energy-scaled contribution from pair production, radiative processes—bremsstrahlung, and photonuclear interactions and $a(E)$ represents electronic stopping power. However, for the energy ranges observed in this report $\sim 10^{-1}GeV$, one can neglect the $b(E)E$ interaction as its contribution is less than 1% [14].

The equation essentially asserts that the penetration capability of muons is determined by their momentum, and the distance of penetration is intricately linked to electronic factors $a(E)$, encompassing properties such as the atomic number and mass composition of the medium through which they traverse [13].

3 Methods

3.1 Detector Specifications & Calibration

The complete instrument used for all experiments required two hardware components: a **Detector Module** and a **Readout Electronics Module**. These would then connect to a PC via USB connection with a custom communication protocol and a data acquisition software would save the data [4]. Fig. 2 below shows the main components of the setup.

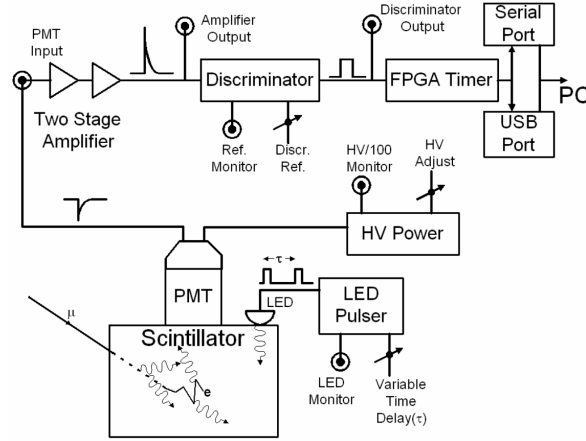


Figure 2: Circuit diagram of muon detector device [4].

Detector Module

To understand Fig 2, an anodized aluminium cylinder contains the entire detector module including the carbon scintillator, a photo-multiplier tube (PMT), and a variable high voltage power supply (HV). The scintillator made out of carbon is optically coupled to a PMT cell. The variable HV is used to power the PMT and is manually controlled and calibrated using a voltmeter. The (HV) calibration procedure determines the voltage threshold where the PMT becomes overly sensitive, leading to over-triggering [4], as depicted in the calibration plot in Figure 3 where there is a sudden change in gradient.

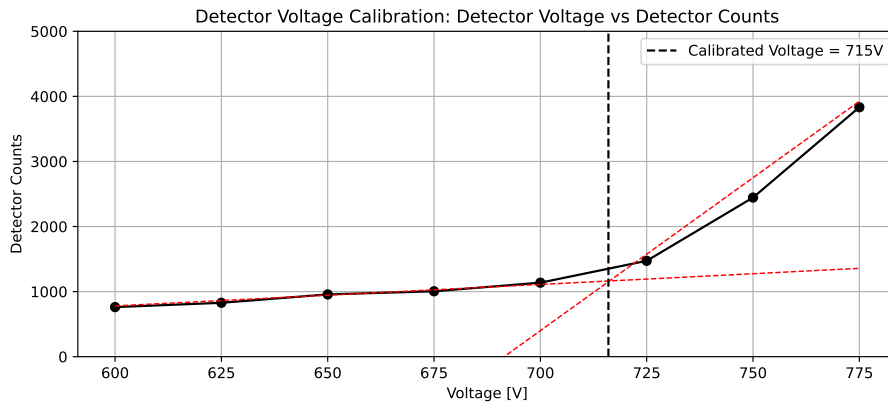


Figure 3: Detector (HV) Calibration plot. Two lines indicate the change in gradient.

Therefore, one calibrates the high voltage supply to be the intersection of these two changes of gradient, in this case, $V_{(HV)} = 715V$.

Readout Electronics Module

The electronics module contains all the electronics necessary to conduct the experiment. The PMT flashes are first amplified and then contrasted against an adjustable threshold, in this case, set to a constant $V_{Threshold} = 296mV$. Flashes above the threshold are measured by time-specific circuitry called the FPGA chip, (field programmable gate array). The first pulse of the detector starts the timing mechanism. If another pulse takes place within $20\mu s$ of the first, the readout equipment measures the time between the two pulses (signalling a muon decay). If no second pulse occurs within $20\mu s$, the pulse is measured as a muon that passes through the detector. Communication circuitry then transfers the time-stamped data to a PC through a USB port [4].

3.2 Raw Data Processing

The scintillator output raw data comprises of two columns encoding muon events, and their corresponding Unix time stamps respectively. To illustrate, we have the following raw data as an example:

```
40001 1624891836
260 1624891837
40005 1624891837
```

If the first field begins with an integer larger than “40000”, signifying a timeout, the last two digits (representing muon counts in one second) are extracted and added to the total muon count array. On the other hand, numbers below “40000” denote the decay time for a muon in ns, and these values are appended to the muon decay count array. Both processed detection counts and decay counts are stored in separate lists with their corresponding timestamps [4].

For each of the subsequent experiments below, custom Python files used the same reading and processing technique and were used to create all the plots. All of these files can be found organised in the GitHub repository¹ together with all the graphs and raw data used.

¹<https://github.com/05patrickn/Senior-Honours-Muon-Decay>

4 Experiment 1 - Muon Counts After Solar Flares

4.1 Experimental Setup

Throughout the project’s lifetime, no X-Class solar flares occurred [10]. Consequently, a Python script was developed to analyze all the muon data ever collected by the equipment in the quest to find solar flares. Utilizing the Space Weather Catalogue’s database of solar flares, the code identified a total of 13 solar flares in the data [10]. Out of these detected events, only 6 exhibited a noticeable Forbush decrease. These Forbush decreases were observed during a period of heightened solar activity from October 25th to November 10th, 2013. Therefore, the report will concentrate on analyzing the events that occurred during this time frame, as the detector remained fully operational throughout, maintaining consistent calibration parameters, albeit with unknown specific values.

4.2 Results & Analysis

The first plot analyzed within this time frame was associated with an X2.3 flare. In this case, a 3-bin rolling mean was used within 45-minute bins. The choice of a 3-unit window rolling mean was used as it struck an optimal balance between smoothing the time-series data, and retaining relevant trends whilst also not overcrowding the plot [15].

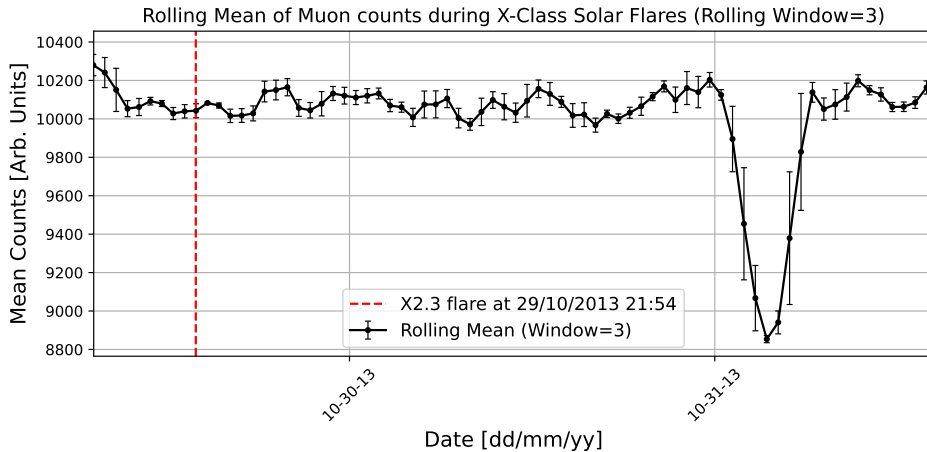


Figure 4: Variation of muon counts in 45-minute bins in the event of an X2.3 solar flare; error bars are the standard error within each bin.

In Figure 4, we observe a 14% reduction in muon counts, aligning with the anticipated X2.3 solar flare. This Forbush decrease falls within the documented range in the literature, spanning from a 3% to a 20% count reduction [12]. Notably, this decline also represents a significant statistical deviation of $\sim 8\sigma$ from the mean count, effectively eliminating the possibility of statistical fluctuations.

Another point of interest lies in the time gap between the flare and the peak of the Forbush decrease, which, in this instance, amounts to 39 hours following the initial event.

However, this time lag varies largely from one event to another. Figure 5 below illustrates the differing delays associated with an X3.3 and X1.1 event.

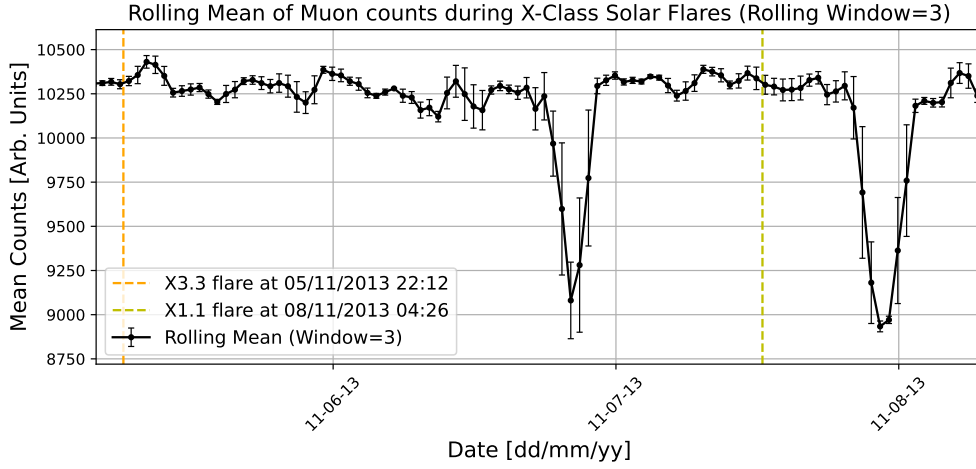


Figure 5: Variation muon counts in 45-minute bins in the event of an X3.3 and X1.1 solar flare; error bars are the standard error within each bin.

As mentioned, the varying time lengths between solar flares and Forbush decreases are evidently clear in Figure 5, whereby there is a 29 and 10-hour time lag between the X3.3 and X1.1 events respectively. This is thought to be caused by several factors including the solar wind, the associated mass ejection speed, direction of propagation, magnetic field interactions and the composition and density of the solar wind [11, 12]. However, the precise nature of this interaction still remains largely unknown.

On a separate note, some flares that were expected to give the dips in data were not clearly matched with a Forbush decrease as shown below by Figure 6.

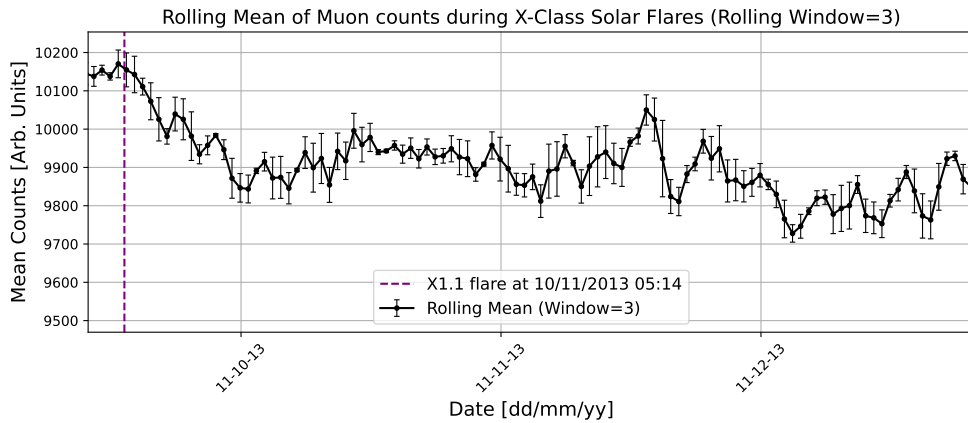


Figure 6: Anomalous behaviour with no Forbush decrease. Muon counts in 45-minute bins in the event of an X1.1 solar flare; error bars are the standard error within each bin.

As mentioned, not all solar flares are accompanied by Forbush decreases. Out of the 13 total detected solar flares, only 6 were associated with a Forbush decrease, indicating that less than half (46%) of them exhibit this phenomenon. The precise cause that triggers this phenomenon also remains unknown. However, it is theorized that it could be linked to variations in the injections of solar plasma and variations of the impact of the shock wave on Earth's magnetic field, affecting cosmic ray intensity in different ways [6].

5 Experiment 2 - Muon Momentum Spectra

5.1 Experimental Setup

The second experiment aimed to reconstruct the momentum spectra of the cosmic ray muons entering the scintillator. To be able to do so, steel plates of density $\rho = 7.874g/cm^3$ and dimensions of 32x32x0.5cm were stacked one on top of another just above the muon scintillator using a steel frame to hold these. The experiment then ran consecutive 10-minute sampling measurements where the number of plates above the detector increased by 10 plates each time from a total of 50 stacked plates. From these 10-minute sampling periods, the total count number was sampled and plotted.

5.2 Results & Analysis

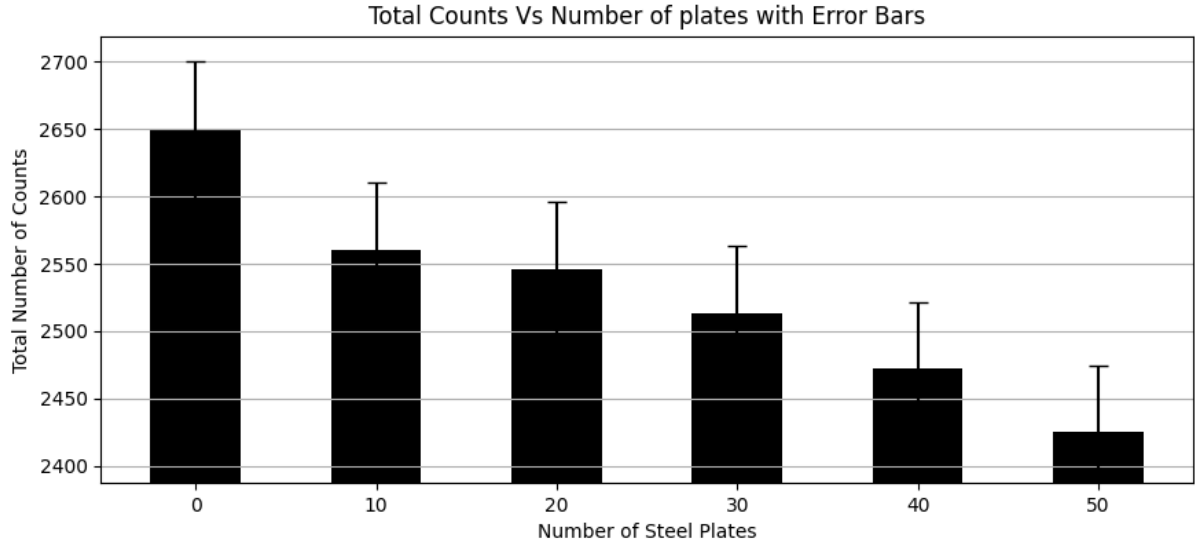


Figure 7: Variation of muon counts with varying number steel plates. Error bars based off Poisson statistics to be \sqrt{counts} .

As shown in Figure. 7 muon counts detected are influenced by the mass of material above the detector. This effect occurs when negative muons are captured by atomic nuclei, resulting in a reduced flow of muons entering the scintillator. Therefore, increasing the number of steel plates is expected to lead to a decrease in the muon counts [16].

Then, by examining the difference in counts between experiments with 10 plates (C_{10}) and those without any plates (C_0), and subsequently multiplying this difference by the thickness of the plates, we obtain the differential counts with respect to penetration depth.

The mathematical representation of this relationship is given by:

$$\text{Differential Counts} = (\Delta C) \times \text{Plate Thickness} \quad (7)$$

where $\Delta C = C_{10} - C_0$ represents the difference in counts between consecutive experiments and the Plate Thickness is known to be 0.5cm. Then by using the data tables from D.E Groom *et al.* which connect the penetration depth to the muon momentum, one can obtain a plot of the differential counts with respect to muon momentum [14]. Then by normalising the differential counts, we obtain the following plot of the muon momentum against differential intensity and compare these against literature results:

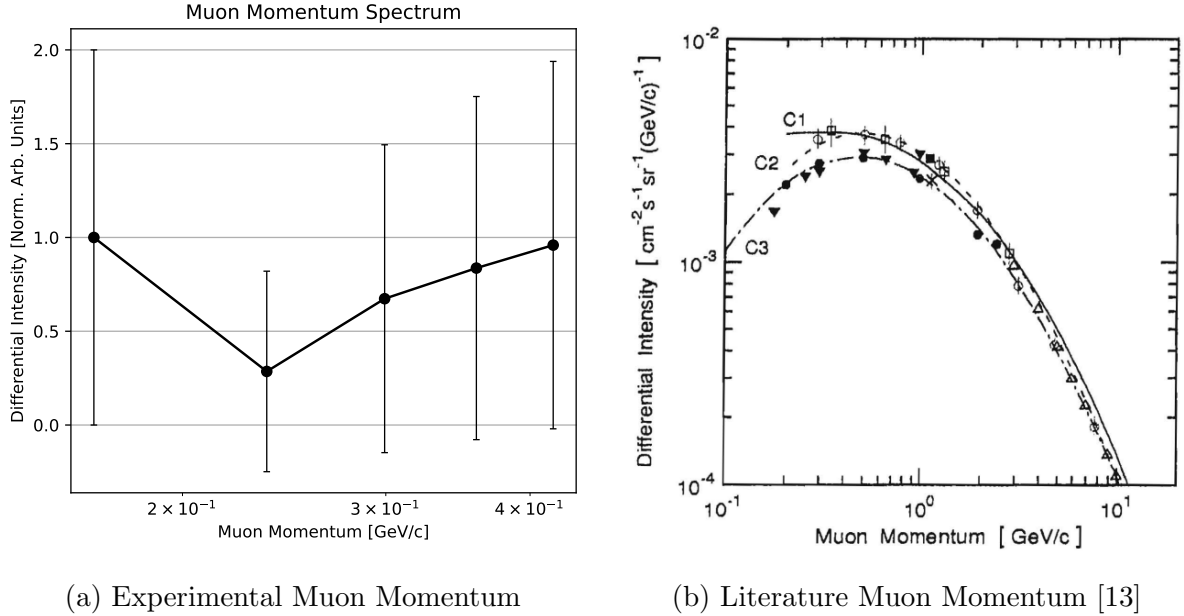


Figure 8: Comparison of Normalized Differential Intensity versus Muon Momentum; Error bars based on Poisson statistics for decays, $\sqrt{\text{counts}}$.

As depicted in Figure 8(a), a clear anomaly is observed in the first data point, where the differential intensity deviates noticeably from the anticipated curved trend as illustrated in plot (b) from the literature expectation. While it may be tempting to re-take the data or discard this data point altogether, it is worth to note that the anomaly could be attributed to the unique scenario it represents: measuring the differential between the absence (0) and presence of 10 plates. Therefore, it is hypothesized that the initial interaction of muons with the first steel plates might result in an unusually large differential. [16, 14]

Nevertheless, it is essential to acknowledge that this hypothesis warrants further experimentation to validate. But apart from the anomaly, the data closely aligns with the expectations from the literature for low momentum ranges. Whereby the curve exhibits a gradual descent, reaching a peak around 500 MeV/c [4, 13].

6 Experiment 3 - Muon Count Vs. Pressure

6.1 Experimental Setup

Another significant parameter determining the muon detection is attributed to meteorological effects. Current research from Savić *et al.* shows that one of the main contributors to muon counts is barometric effects [17].

Therefore for this experiment, 2-week-long data during a time frame of geomagnetic quiet days (no large solar flares) was chosen to be from the 17th to the 31st of October 2023 [18]. The muon counts from this time frame are then placed into 15-minute bins. These 15-minute muon count bins are then associated with the corresponding 15-minute interval barometric readings from an Easylog EL-SIE-6+ barometric reader [19]. By binning the data a second time into 20 equal bins to not over-crowd the plot, we obtain the following.

6.2 Results & Analysis

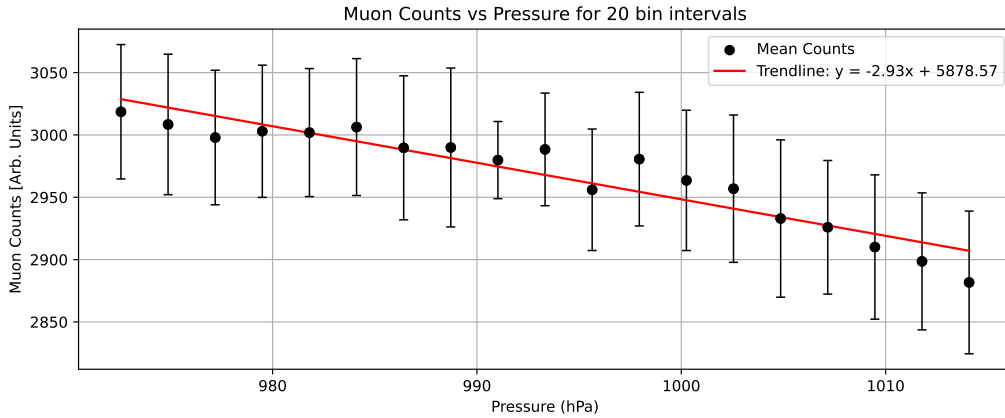


Figure 9: Plot of the variation of the number of counts against pressure over 20 equal bins; error bars show the standard error within each bin. The line is a linear least square fit.

Figure 9 illustrates a weak negative correlation between atmospheric pressure and observed muon counts. This aligns with the expectation that increased air mass leads to greater muon energy loss and decay before reaching the detector. Similar to the metal shielding experiment, fluctuations in counts are attributed to mass variations above the detector due to atomic capture of negative muons, resulting in a reduced influx and increased energy loss before reaching the detector [20].

While there appears to be a connection supporting the initial hypothesis that atmospheric pressure changes impact muon counts, the presence of significant error bars in the data emphasizes the need for further investigation and data refinement. A plot of the residuals is presented below:

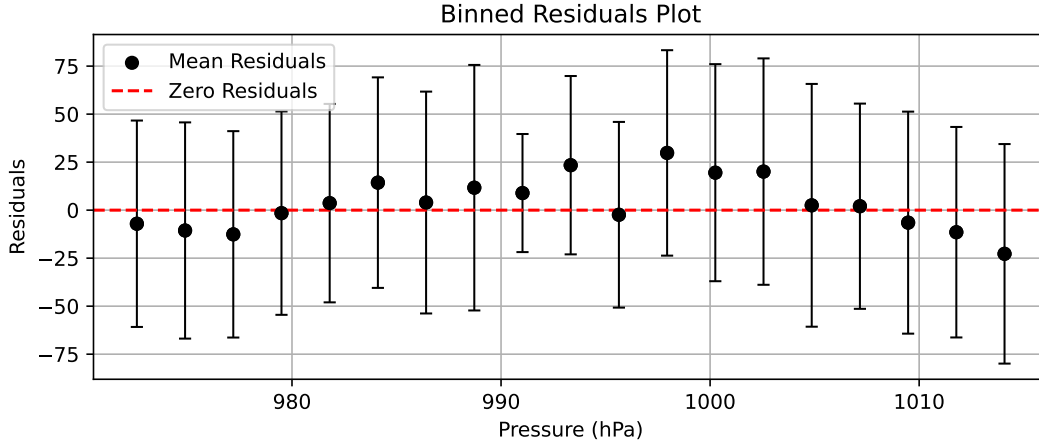


Figure 10: Residuals from the linear least square fit of binned muon counts against pressure. Error bars show the standard error within each bin.

Examining the residuals reveals what appears to be a wave-like behaviour. To draw conclusive insights and achieve a more comprehensive understanding of the relationship between these variables, additional statistical analyses and repeated measurements may prove beneficial. While the existing data suggests a potential trend, its precision falls short of constructing a reliable trend line for correcting future data. When comparing to various other experimental results, the general overall trend is observed and shared, whereby a lack of precision is commonplace. The barometric coefficient (trend-line gradient) exhibits too much underlying noise to be determined precisely. J. Poirier et al., upon repeating this experiment, found that the “fits reveal a wide range of possible barometric correction coefficients ranging from -0.50 to -1.65” [20]. Therefore, unless more precise equipment is obtained, the current results will remain the same.

7 Experiment 4 - Muon Decay Half-life

7.1 Experimental Setup

The final experiment aimed to determine a precise value for the positive muon half-life. To gain the most accurate value possible, a year-long data sample of decay counts from the equipment were analysed [1].

7.2 Results & Analysis

Throughout the analysis, various fitting libraries and techniques, including binned and unbinned least-square and maximum likelihood fits, were tested. From these, an unbinned least square fit on the data provided the best fit and residuals and hence was chosen. At the same time, various correction terms on the exponential decay function were also examined in search of the best fit and residuals. This led to the following optimisation function:

$$A * \text{np.exp}(-x / \text{tau}) + m * x + C$$

The decision to include a linear term ($m*x+c$) in the background not only offered significant improvements to the residuals but was also motivated by the fact that the detector registers particles—whether charged (e.g., electrons, muons) or neutral (e.g., photons)—based on scintillation light. The detector cannot differentiate between light generated by stopping muons and decaying muons inside the detector and that created by consecutive through-going muons, resulting in the need for a background.

Furthermore, to address imbalances in the residuals adversely affecting the fit, the minimum decay time was adjusted to 1450 ns. This modification proved crucial in rectifying residuals as low decay times skewed the residuals towards higher counts.

After all these corrections and considerations in mind, one obtains the following plots.

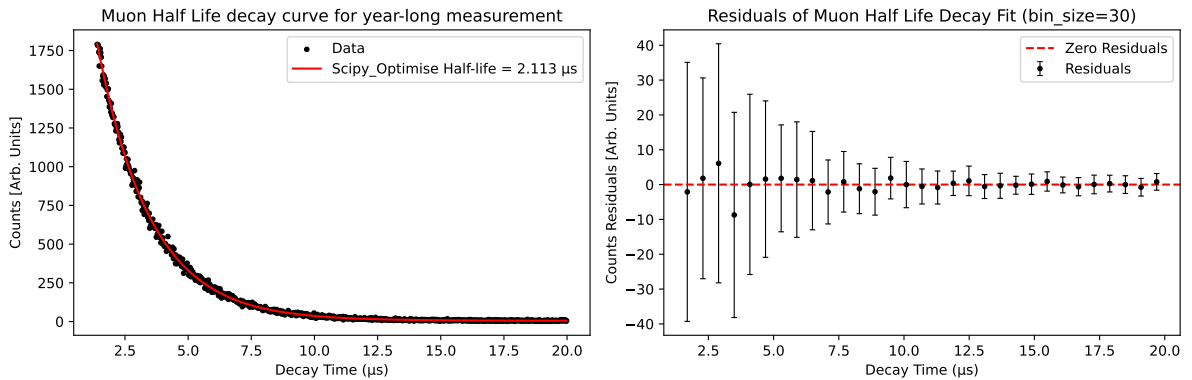


Figure 11: On the left, an unbinned plot illustrating Muon Decay Events, accompanied by a least square fit yielding $\tau_{\text{obs}} = 2.113 \pm 0.008 \mu\text{s}$. On the right, a residual plot organized into 30 equally spaced bins; the error bars depict the standard error within each bin.

A least square fit analysis was performed on Figure 11 to ascertain the observed muon half-life, resulting in the value: $\tau_{\text{obs}} = 2.113 \pm 0.008 \mu\text{s}$. The claimed uncertainty is calculated from the propagated standard error within the binned residuals.

Therefore, in order to obtain the “free space value” given that the scintillator detects both positive and negative muon decay τ_{obs} . We resort to splitting the half-life using the muon flux ratio equation derived in Appendix A to find τ^+ .

$$\tau^+ = \frac{\rho\tau^-\tau_{\text{obs}}}{\rho\tau^- + \tau^- - \tau_{\text{obs}}} \quad (8)$$

Where we have parameters obtained from the experiment and other experimental results obtained from Cern Experiments and UC Davis to be as follows [3, 21]:

$$\begin{aligned} \tau^- &= 2.0398 \pm 0.0008 \mu\text{s} \text{ (Carbon)} \\ \rho &= 1.2766 \pm 0.0032 \\ \tau_{\text{obs}} &= 2.113 \pm 0.008 \mu\text{s} \end{aligned}$$

Plugging these values into (8) and propagating the errors respectively results in a “free space value” of $\tau^+ = 2.174 \pm 0.015 \mu\text{s}$. These findings are in decent agreement with the literature value of $\tau_{\text{Literature}}^+ = 2.1969811 \pm 0.0000022 \mu\text{s}$ falling within a 1% systematic error [3]. The source of this small systematic error can be attributed to the challenges in accurately estimating the negative half-life of the carbon scintillator, assuming the flux ratio at the scintillator itself is $\rho = 1.2766 \pm 0.0032$ and mostly noise in the plot of decay curve.

7.2.1 Fermi Coupling Constant

The decay process of τ^+ obtained above, which exclusively occurs through the weak force, provides a precise means to measure the strength of the weak force interaction [8]. The Fermi Coupling constant (G_F), representing this weak force interaction, can be accurately calculated using the following formula:

$$G_F = \sqrt{\frac{192\pi^3\hbar}{\tau^+m^5c^4}} \quad (9)$$

Here, τ^+ is the decay time of the process, m is the muon rest mass, \hbar is the reduced Planck constant, and c is the speed of light. This expression allows us to quantitatively determine the Fermi Coupling constant based on experimental results. By using the following parameters in natural units:

$$\begin{aligned} \tau^+ &= 2.174 \times 10^{-6} \text{ s} \\ \Delta\tau^+ &= 0.015 \times 10^{-6} \text{ s} \\ \hbar &= 6.582 \times 10^{-25} \text{ GeV s} \\ m_\mu &= 0.10566 \text{ GeV} \\ c &= 1 \text{ (speed of light)} \end{aligned}$$

And by substituting the given values, one obtains:

$$G_F = 1.169 \times 10^{-5} \text{ GeV}^{-5}$$

Regarding the uncertainty in G_F , the uncertainty of the other parameters are taken to be negligible and using the uncertainty propagation formula:

$$\delta G_F = G_F \sqrt{\left(\frac{\Delta \tau^+}{\tau^+}\right)^2} = 8 \times 10^{-8} \text{ GeV}^{-5}$$

The Fermi coupling constant, calculated as $1.169 \pm 0.008 \times 10^{-5} \text{ GeV}^{-5}$, exhibits a discrepancy from the literature value of $1.16639 \times 10^{-5} \text{ GeV}^{-5}$ of about 0.2%. This deviation demonstrates that the interaction for from the measured τ^+ is highly dominated by the weak force.

8 Conclusion

The analysis of muon data during the heightened solar activity period from October 25th to November 10th, 2013, revealed insights into solar flares and Forbush decreases. Out of 13 solar flares identified, only 6 exhibited Forbush decreases. Varying time lags between solar flares and decreases underscored complexity, influenced by supposed factors like solar wind and magnetic interactions. Some flares lacked Forbush decreases, emphasizing the nuanced nature of cosmic-ray modulation. Continued experimentation would be encouraged in extending the duration of measurements and capturing additional data such as cosmic ray flux, solar wind speeds or magnetic storms. As the examination of this additional data may contribute to uncovering new insights or clarifying underlying mechanisms.

The second experiment aimed to reconstruct cosmic ray muon momentum spectra using stacked steel plates as shielding. Analysis of the differential counts with respect to the penetration depth revealed an anomaly in the initial data point, potentially linked to the unique interaction with the first set of plates. Further investigations, particularly into the anomalous data point, could provide a comprehensive understanding of muon interactions with shielding materials at the low limit.

The third experiment looking at data on atmospheric pressure and muon counts suggests a potential correlation, although further refinement and statistical analysis are essential to establish a more robust relationship between these variables. However, it is likely that the barometric coefficient for data correction will not be able to be accurately determined anytime soon due to the underlying noise of the associated physics itself.

Finally, the determination of the positive muon half-life as $\tau^+ = 2.174 \pm 0.015 \mu s$ exhibits a good agreement with the literature value. The utilization of a least square analysis, along with careful consideration of residuals, greatly helped enhance the accuracy in determining the observed muon half-life. Additionally, this data provided an accurate

estimate for the Fermi Coupling constant calculated as $1.169 \pm 0.008 \times 10^{-5}$ with a percentage error of 0.2% underlying the fact that the τ^+ interacts mainly through the weak force.

Overall, the observed trends not only deepened our understanding of muon physics, astrophysical and meteorological effects but also opened new avenues for further exploration and refinement of experimental methodologies. These results serve as a solid foundation for comprehending muon behaviour in diverse exotic conditions, offering potential applications in various scientific domains like meteorology and astronomy.

9 Acknowledgements

I would like to thank my supervisor Dr. Matthew Needham for his endless patience and help with all my questions.

10 References

- [1] B. L. Robert, “Muon Physics: A Pillar of the Standard Model” arXiv:0704.2394 (2007) pg1-8.
- [2] T. P. Gorringer, D.W. Hertzog “Precision Muon Physics” arXiv:1506.01465v1 (2015) pg3-27.
- [3] J. Beringer *et al.*, “LEPTONS” Particle Data Group PR D86, 010001 (2012) pg1-10.
- [4] T.E. Coan, J. Ye, “Muon Physics MPI-A USER’S MANUAL” Teach Spin (2009) pg1-29.
- [5] M.F. Shopova, Prof. P Iaydjiev, “PERFORMANCE OF THE CMS RPC SYSTEM – FROM LS1 UPGRADE TO RUN2 AT LHC” Cern-Thesis-2018-080 (2018) pg16-17.
- [6] Prof. B. Rossi, “Cosmic Rays” Library of Congress Catalog Card Number 64-17570 (1964) pg 210-215.
- [7] V. Khachatryan *et al.*, “Measurement of the charge ratio of atmospheric muons with the CMS detector” CMS-MUO-10-001 (2010) pg1-15.
- [8] A. G. Bryer, “Measurement of the Positive Muon Lifetime and Determination of the Fermi Constant to Part-per-Million Precision” arXiv:1010.0991v1 (2010) pg 1-9.
- [9] T.Bai, P.A. Sturrock, “Classification of Solar Flares” Stanford University Annual Review of Astronomy and Astrophysics 27(1) (1989) pg34-48.
- [10] S. Vancanneyt *et al.*, “Top 50 solar flares Archive” SpaceWeatherLive.com (2023) (DATABASE. Data accessed: 20/11/2023).
- [11] J. Poirier *et al.*, “A study of the Forbush decrease event of September 11, 2005 with GRAND” Physics Department, University of Notre Dame (2005) pg1-4.
- [12] C. D’Andrea, “ANALYSIS OF GROUND LEVEL MUONS, SOLAR FLARES, AND FORBUSH DECREASES” UMI Publishing UMI Number: 3406974 (2006) pg 72-98.
- [13] P.K.F. Greider, “Cosmic Rays At Eath” ISBN 0-444-50710-8 British Library (2001) pg 254.
- [14] D.E. Groom *et al.*, “MUON STOPPING POWER AND RANGE TABLES 10 MeV–100 TeV” Atomic Data and Nuclear Data Tables 78, 183–356 (2001) pg 63.
- [15] H.H. Hameed, “Smoothing Techniques for Time Series Forecasting ” Eastern Mediterranean University (2015) pg 8-15.
- [16] M Gardener *et al.*, “The Momentum Spectrum of Cosmic Ray Muons near Sea Level in the Momentum Range 0.4-10 GeV/c” Proc. Phys. Soc. 80 697 (1962) pg 2-14.
- [17] M. Savić *et al.*, “Pressure and temperature effect corrections of atmospheric muon data in the Belgrade cosmic-ray station” J. Phys.: Conf. Ser. 632 012059 (2015) pg1-8.

- [18] H.F. Johnston, “INTERNATIONAL Q-DAYS AND D-DAYS” International Service of Geomagnetic Indices (2023) (DATABASE. Data accessed: 11/11/2023).
- [19] Easy Log Datasheet, “EL-SIE-6+ High Accuracy Temperature, Humidity and Pressure USB Data Logger” Lascar Electronics (2022).
- [20] J. Poirier, T. Catanach, ”Atmospheric Effects on Muon Flux at Project GRAND” Physics Department, University of Notre Dame DOI: 10.7529/ICRC2011/V11/0307 (2011) pg1-4.
- [21] D.F. Measday *et al.*, “Total nuclear capture rates for negative muons” University of British Columbia Volume 35, Number 6 (1987) pg 6.

A Appendix: Derivation of τ^+

Let λ^- represent the decay rate for the μ^- in the carbon plastic scintillator, and let λ^+ be the decay rate for positively charged muons. If N^- and N^+ represent the flux of positive and negative muons incident on the scintillator, then the average observed decay rate λ_{obs} is given by:

$$\lambda_{\text{obs}} = \frac{N^+\lambda^+ + N^-\lambda^-}{N^+ + N^-} \quad (10)$$

Now, let's define $\frac{N^+}{N^-}$ as ρ , where ρ is the flux ratio, a known quantity and substitute:

$$\lambda_{\text{obs}} = \frac{\rho\lambda^+ + \lambda^-}{1 + \rho} \quad (11)$$

Now we take the reciprocal whereby $\tau_{\text{obs}} \equiv (\lambda_{\text{obs}})^{-1}$, substitute and we obtain:

$$\tau_{\text{obs}} = \frac{1 + \rho}{\rho\lambda^+ + \lambda^-} \quad (12)$$

Similarly, $\tau^+ \equiv (\lambda^+)^{-1}$ and $\tau^- \equiv (\lambda^-)^{-1}$ can be substituted giving:

$$\tau_{\text{obs}} = (1 + \rho)\left(\frac{1}{\tau^-} + \frac{\rho}{\tau^+}\right)^{-1} \quad (13)$$

Rearranging for τ^+ :

$$\frac{\tau_{\text{obs}}}{(1 + \rho)} = \left(\frac{1}{\tau^-} + \frac{\rho}{\tau^+}\right)^{-1} \quad (14)$$

$$\frac{(1 + \rho)}{\tau_{\text{obs}}} = \left(\frac{1}{\tau^-} + \frac{\rho}{\tau^+}\right) \quad (15)$$

$$\frac{(1 + \rho)}{\tau_{\text{obs}}} - \frac{1}{\tau^-} = \frac{\rho}{\tau^+} \quad (16)$$

$$\frac{\tau^-(1 + \rho) - \tau_{\text{obs}}}{\tau^- \tau_{\text{obs}}} = \frac{\rho}{\tau^+} \quad (17)$$

Thus giving us the final equation:

$$\tau^+ = \frac{\rho\tau^-\tau_{\text{obs}}}{\tau^-(\rho + 1) - \tau_{\text{obs}}} \quad (18)$$

B Appendix: Complete Solar Flare Data 2013

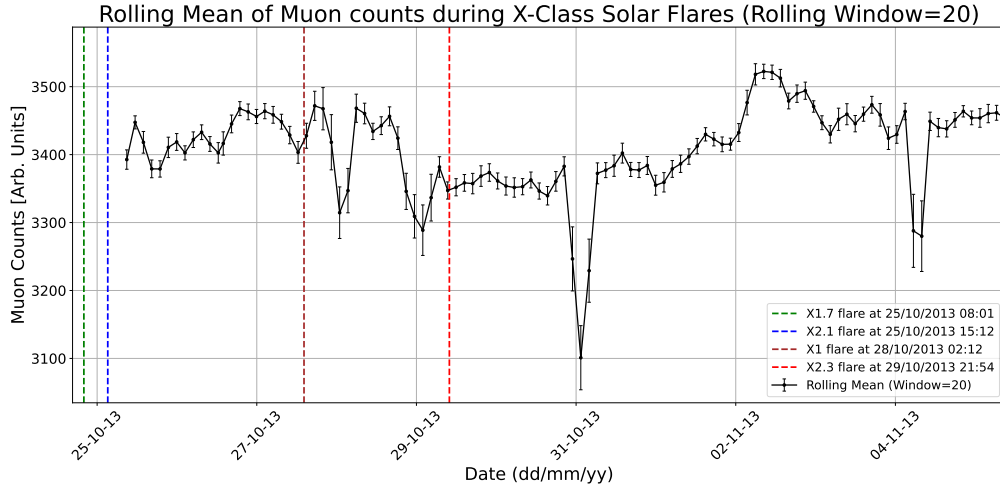


Figure 12: Variation of muon counts in 15-minute bins in the event of various solar flares; error bars are the standard error within each bin.
(Time window from 25/10/2013 : 04/11/2013)

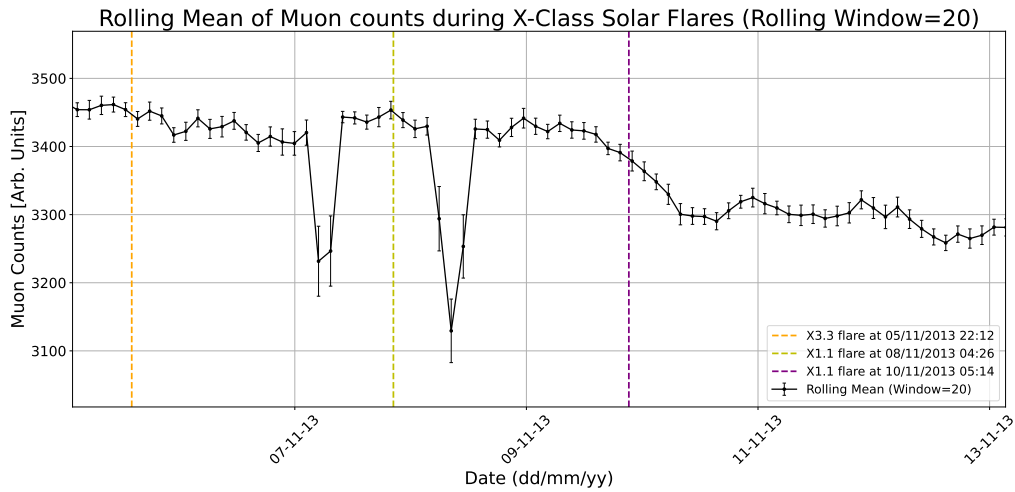


Figure 13: Variation of muon counts in 15-minute bins in the event of various solar flares; error bars are the standard error within each bin. Note no Forbush decrease after X1.1 Flare on 10/11/2013.
(Time window from 05/11/2013 : 13/11/2013).